Anisotropic failure modes of high-strength aluminium alloy under various stress states

M. Fourmeau[a,b,*], T. Børvik[a], A. Benallal[b] and O.S. Hopperstad[a]

[a] *Structural Impact Laboratory (SIMLab), Centre for Research-based Innovation (CRI) and Department of Structural Engineering, Norwegian University of Science and Technology, Rich. Birkelands vei 1A, NO-7491 Trondheim, Norway*

[b] *LMT-Cachan, ENS de Cachan/CNRS/UPMC/PRES Universud, 61, avenue du Président Wilson, 94235 Cachan cedex, France*

Abstract

The influence of stress state and plastic anisotropy on the fracture behaviour of a rolled AA7075-T651 aluminium plate under quasi-static loading conditions is studied both experimentally and numerically. Material tests in different directions of the plate were carried out using specimens with various shapes to provide a wide range of stress states. The strain to failure and the failure modes were found to vary strongly with the stress state, but also with the loading direction due to the complex microstructure of the alloy. Finite element simulations adopting an anisotropic plasticity model were used to obtain local values of stresses and strains and to define the strains at fracture for the various stress states. The numerical simulations show that due to the heterogeneous stress and strain fields in the specimens, it is very difficult to accurately locate the point where fracture initiates and thus to determine the local fracture strain as a function of stress state and loading direction.

Keywords: A Fracture; B Anisotropic material; Metallic material; C Mechanical testing; Finite elements

---

[*] Corresponding author. Tel.: + 47-73-59-46-90; fax: + 47-73-59-47-01.

E-mail address: marion.fourmeau@ntnu.no

1. Introduction

For the last decades, components made of high-strength aluminium alloys have been increasingly used by the industry. Such components are obtained after various manufacturing operations, e.g. extrusion and rolling processes, which impose extremely large deformations to the material. These operations may lead to strongly anisotropic properties, which cannot always be neglected if one wishes to correctly represent the mechanical behaviour of the processed material. For such high-strength aluminium alloys, the modelling of fracture becomes important as the strength is obtained at the expense of ductility.

Nucleation, growth and coalescence of voids are known to be the mechanisms responsible for ductile failure. The growth mechanism was first described analytically for an infinite perfectly plastic isotropic medium containing either a cylindrical void by McClintock (1968) or a spherical void by Rice and Tracey (1969). These studies revealed that the growth of a void (and consequently the fracture) is controlled by the stress triaxiality factor and the plastic strain intensity. Later, Gurson (1977) derived an expression for the yield locus of an isotropic medium containing a spherical void. Since these pioneering works, the description of the void growth mechanism has been enriched in many different ways, as outlined in a recent review by Lecarme et al. (2011). Criteria describing nucleation and coalescence of voids were included in the Gurson model by Chu and Needleman (1980) and Tvergaard and Needleman (1984), leading to the well-known GTN model. The void shape effect was introduced in the Gurson model by Gologanu et al. (1993–1994). In parallel, the distribution of spherical voids in an isotropic matrix has been numerically investigated by Gologanu et al. (1994), showing that an anisotropic distribution could influence the coalescence process. More recently, Pardoen and Hutchinson (2000) proposed to couple this model with the Thomason criterion (Thomason, 1990) for void coalescence.

At lower and negative stress triaxiality states or shear dominated loading, fracture often occurs by shear localization. Efforts have been made to reproduce experimental observations at lower stress triaxiality states. These models are often empirical, since the physics of the underlying fracture process is not clearly identified. For instance, Khan and Liu (2012) proposed a new empirical failure criterion based on the relationship between the hydrostatic pressure and the magnitude of the stress vector and obtained better results than with other well-established criteria, such as the maximum shear stress criterion (Stoughton and Yoon, 2011), the J_2-based criterion and the Xue-Wierzbicki criterion (Wierzbicki et al., 2005). Based on experimental tests at low stress triaxialities, Bao and Wierzbicki (2004) observed that the strain to failure drops at stress triaxialities close to zero. They proposed to distinguish between void growth, which is predominant at high stress triaxialities, and shear fracture, which dominates at low stress triaxialities. Barsoum and Faleskog (2007) have shown experimentally the influence of the third invariant of the deviatoric stress tensor on ductile failure, while Nahshon and Hutchinson (2008) introduced the third invariant in the Gurson model to reproduce the shear dominated failure mode observed at low stress triaxiality states. To introduce the influence of the third invariant, Bai and Wierzbicki (2010) proposed a modified Mohr-Coulomb fracture criterion formulated in the space of stress triaxiality, Lode angle and equivalent plastic strain. Dunand and Mohr (2011) showed the capabilities of such models to predict fracture of an aluminium alloy over a large range of stress triaxialities and values of the Lode parameter.

Since metallic alloys often are provided as extruded or rolled plates, another important aspect of the material behaviour is the deformation-induced plastic anisotropy. The yielding behaviour is found to strongly depend on the loading direction with respect to the principal directions of anisotropy of the material. In addition to anisotropic yielding (Hill, 1948; Barlat et al., 2005; Rousselier et al., 2012), some alloys also show anisotropic failure (Chen et al., 2009). A numerical representation of the microstructure coupled with damage models enabled Steglich et al. (2008) to represent the anisotropic ductile fracture of an aluminium alloy, while Yerra et al. (2010) numerically described the fracture inside a grain using a crystal plasticity material model around a spherical void. Recently, Luo et al. (2012) proposed an anisotropic failure criterion based on a linear transformation of the plastic strain-rate tensor.

Establishing physically based models of the fracture mechanisms requires knowledge about the microstructural features of the material and their involvement in the failure process. For the complex microstructure of high-strength aluminium alloys, such as the AA7075-T651 (Børvik et al., 2010; Pedersen et al., 2011), there is a competition between intragranular and intergranular fracture owing to the existence of precipitate free zones along the grain boundaries. The variety of fracture mechanisms for aluminium alloys have been investigated for more than thirty years, and fracture maps were presented by Teirlinck et al. (1988). Hahn and Rosenfield (1975) pointed out that two populations of particles of different magnitude are involved in the fracture process at different levels. Void growth occurs around large constituent particles, while localization leading to coalescence is facilitated by void growth around smaller dispersoids. They also observed that under certain loading conditions failure can be partly intergranular. Based on tensile tests performed in the three orthotropic directions of a rolled AA7075 aluminium plate and fracture surface observations, Jordon et al. (2009) quantified the influence of two different size-order particle populations (constituent and dispersoids) on the damage process and their anisotropic characteristics. They also proposed a continuum-based damage model enriched by internal variables related to the two populations of particles.

In this paper, rolled plates of the AA7075 aluminium alloy in temper T651 are studied. This alloy belongs to the AlZnMg series and contains precipitates that increase the mechanical properties, such as the yield limit and the tensile strength. Due to the rolling process, the grains are flat and elongated along the rolling and transverse directions, the constituent particles are organized in the rolling plane of the plate, and a crystallographic texture is engendered. Pedersen et al. (2011) microscopically observed the fracture surfaces of this alloy subjected to various quasi-static and dynamic loadings and identified the different failure modes. Assuming orthotropic symmetry, Fourmeau et al. (2011) identified the parameters of the anisotropic yield function Yld2004-18p proposed by Barlat et al. (2005). Tensile tests in different directions of the plate were used, completed by tensile tests on notched specimens, upsetting tests and shear tests. The experimental investigation presented here provides data concerning the failure of the AA7075-T651 aluminium alloy for a wide range of stress states and loading directions. The relation between equivalent strain to failure, stress triaxiality and direction of loading is then quantified and discussed, supported by numerical simulations of the tests.

2. Material AA7075-T651

The studied aluminium alloy is the AA7075 in temper T651. The chemical composition is given in Table 1. This high-strength aluminium alloy has nominal yield limit and tensile strength in the rolling direction equal to 505 MPa and 570 MPa, respectively. All material specimens presented in this study were manufactured from the same 20 mm thick plate. Temper T651 implies that the alloy is slightly stretched and aged to peak strength. The grain structure of the as-received AA7075-T651 plate is shown in Fig. 1 (a), whereas Fig. 1 (b) shows the distribution of the constituent particles in the same planes. The rolling process implies a crystallographic texture and leads to plastic anisotropy (Børvik et al., 2010; Fourmeau et al., 2011).

The AA7075-T651 has a complex microstructure with different classes of particles. Coherent precipitates of $MgZn_2$, the so-called η'-phase, appear during the artificial age hardening to temper T6. These are at the nanometre scale and densely distributed inside the grains. The precipitates contribute to the strain hardening of the material by preventing the dislocation movements (Park and Ardell, 1988). Particles called dispersoids, with a different size (0.05 to 0.15 μm) and composition (Al_3Ti, Al_6Mn, Al_3Zr, $Al_{12}Mg_2Cr$, $Al_{20}Cu_2Mn_3$), act as barriers and limit the recrystallization during tempering (Andreatta et al., 2003). This explains the non-recrystallized grain structure with flat and elongated grains in the rolling plane of the plate. Larger intermetallic iron-based particles called constituent particles (at micrometre scale), such as $Al_6(Fe,Mn)$, Al_3Fe, $Al(Fe,Mn,Si)$ and Al_7Cu_2Fe (or silicon-based such as Mg_2Si) are preferentially distributed along the rolling direction (RD), as shown by Jordon et al. (2009) and illustrated in Fig. 1 (b).

A last but very important microstructural characteristic of the 7xxx series of aluminium alloys is the presence of so-called Precipitate Free Zones (PFZ). These PFZs are very narrow zones (at nanometre scale) created during the tempering operations and are generally located adjacent to the grain and sub grain boundaries (GB). These zones are generally softer compared to the interior of the grains, i.e. the matrix. The softness of the PFZ is caused by the local depletion of vacancies which inhibits the formation of fine dispersion of particles in the crystals. In addition, the local solute depletion is initiated by heterogeneous precipitation of stable phase at the grain boundaries. Experiments indicate that plastic strain can be highly localized inside these soft zones and can therefore significantly reduce the ductility of these materials (Dumont et al., 2003).

3. Experimental investigation

The effects of stress state and loading direction on the fracture behaviour of AA7075-T651 are investigated in the following. Different specimen geometries were used to obtain a wide range of stress states, as shown in Fig. 2. The specimens were sampled in several orientations of the plate to evaluate the anisotropic properties of the material. The tests were performed using various universal testing machines at room temperature and nominal strain-rates at the order of $5.10^{-4}\mathrm{s}^{-1}$ (i.e. quasi-static loading conditions). Time, force and displacement were continuously measured in all tests until fracture occurred.

3.1 Uniaxial tensile tests

Tensile tests were carried out on smooth axisymmetric specimens with a cross-section diameter of 6 mm (see Fig. 2 (a)). The tensile axis was oriented at 0°, 15°, 30°, 45°, 60°, 75° and 90° with respect to the rolling direction of the plate (RD). Additional tests were performed in the thickness direction of the plate (ST) on miniature smooth specimens especially designed for plates of 20 mm thickness (see Fig. 2 (b)). During testing, the diameter at minimum cross-section of the specimen was continuously measured until fracture. This was made possible using a purpose-built measuring rig with two perpendicular lasers that accurately measured the specimen diameter. Each laser projected a beam with dimension $13\times0.1\mathrm{mm}^2$ towards the detector on the opposite side of the specimen. Thus, the two orthogonal lasers created a box of laser light of $13\times13\times0.1\mathrm{mm}^2$ around the minimum cross-section of the sample. As the specimen was deformed, the continuous change in diameters was observed by the detectors. This dual-axis micrometre was made up of a high-speed, contact-less AEROEL XLS13XY laser gauge with 1 µm resolution. The gauge was installed on a mobile frame to ensure that the diameters always were measured at minimum cross-section. During elongation, the sample was scanned at a frequency of 1200 Hz and the measured data was transferred by the built-in electronics to the remote computer via fast Ethernet. The diameters were measured in the thickness direction of the plate (ST) and in the transverse direction of the specimen (TD), denoted D_{ST} and D_{TD}, respectively. For the specimens loaded in the thickness direction, the diameters were measured in the rolling direction (RD) and in the long transverse direction (LT) of the plate, giving D_{RD} and D_{LT}, respectively.

The stress-strain curves for the tensile tests on smooth axisymmetric specimens are presented in

Fig. 3 in terms of Cauchy stress versus logarithmic strain averaged over the minimum cross-section of the specimen. For the in-plane tests in

Fig. 3 (a) a representative curve is plotted for each direction since the scatter with respect to stress level was insignificant. The curves are stopped at the average failure strain found between duplicate tests. For the tests through the thickness of the plate in

Fig. 3 (b) all duplicate tests are shown since the scatter was more pronounced in this case. Stresses and strains are calculated as

$$\sigma = \frac{F}{A}, \quad \varepsilon = \ln\left(\frac{A_0}{A}\right) = \ln\left(\frac{D_0^2}{D_{ST}D_{TD}}\right) \tag{1}$$

where F is the force measured by the load cell in the test machine, and A_0 and D_0 are the initial cross-section area and diameter of the specimen, respectively. The current elliptical area of the specimen is given as $A=\pi D_{ST}\,D_{TD}/4$ for the in-plane tensile tests and as $A=\pi D_{RD}\,D_{LT}/4$ for the tensile test in the thickness direction of the plate. The strain to failure is denoted ε_f. A significant anisotropy of the flow stress is exhibited, and a more detailed analysis of this anisotropy is presented in Fourmeau et al. (2011). The strain to failure is also found to vary markedly with the loading direction. The stress-strain curves for the tests in the thickness direction (ST), presented in Fig. 3 (b), and in the rolling direction (RD) are found to be similar; except around the yielding point, where the yielding is more gradual for the specimens loaded in the thickness direction. A more remarkable difference is the large scatter in the strain to failure observed for the uniaxial tension tests in the thickness direction.

Fig. 4 (a) illustrates the variation of the strain to failure ε_f with the direction of loading, i.e. for the seven in-plane directions, $\alpha \in \left[0°;90°\right]$, and the thickness direction of the plate (ST). The average values of the strain to failure are presented with error bars indicating the range, i.e. the minimum and maximum values from parallel tests. The figure also shows the strain ratio R_α, defined for the loading direction α as

$$R_\alpha = \left.\frac{\dot{\varepsilon}^p_{TD}}{\dot{\varepsilon}^p_{ST}}\right|_\alpha \tag{2}$$

where $\dot{\varepsilon}^p_{TD}$ and $\dot{\varepsilon}^p_{ST}$ are the logarithmic plastic strain rates in the transverse direction (TD) of the specimen and in the thickness direction of the plate (ST), respectively. For the tests in the through-thickness direction (ST), the strain ratio R_{ST} is defined as the ratio between $\dot{\varepsilon}^p_{RD}$ and $\dot{\varepsilon}^p_{LT}$, i.e. the logarithmic plastic strain rates in the rolling direction (RD) and in the long transverse direction (LT) of the plate, respectively. The value of R_α for each test was determined by averaging over the plastic regime, while the error bars represent the range. It should, however, be noted that in the ST direction, the strain ratio varied substantially within each test, and for this direction the average value was calculated after stabilization, which occurred around a plastic strain of 0.05. Fig. 4 (a) shows that the anisotropy of strain to failure is intimately related to the anisotropy of the strain ratio: the lower the strain ratio, the lower is the strain to failure.

The different fracture modes obtained during the uniaxial tensile tests are presented in Fig. 4 (b). For the tests showing the lowest failure strains (i.e. those performed in the 0° and 90° directions), fracture occurred in a shear mode with the fracture surface oriented at approximately 45° with respect to the loading direction (Pedersen et al., 2011). On the contrary, for tests showing the largest failure strains (tests performed in the 45° and 60° directions), the fracture surface tends to have a cup-and-cone shape. For the loading directions showing intermediate fracture strains (15°, 30° and 75°), fracture occurred in a disrupted shear mode. Most fracture surfaces obtained from tensile tests in the thickness direction (ST) were orthogonal to the specimen axis. The micrograph of one of these fracture surfaces presented in Fig. 5 reveals that fracture occurred along the grain boundaries in the rolling plane. The large scatter obtained in the strain to failure for these specimens (with a diameter of 3 mm, Fig. 2 (b)) may be attributed to the fact that their cross-sections contain only few grains.

3.2 Tensile tests on notched specimens

Notched axisymmetric specimens (see Fig. 2 (c)) were sampled in the 0°, 45° and 90° directions with respect to RD, using two different notch root radii, $R = 2.0\ \mathrm{mm}$ and $R = 0.8\ \mathrm{mm}$. The same experimental procedure as for tensile tests on smooth axisymmetric specimen was used, and stress and strain are computed according to Eq. (1).

Fig. 6 (a) shows the Cauchy stress versus logarithmic strain curves for specimens loaded in the three directions for the two notch root radii as well as for the smooth specimens. The scatter between duplicate tests with respect to stress level was negligible and thus only representative curves are shown in the figure. The curves are stopped at the average strain to failure obtained from the duplicate tests. The introduction of a notch in the tensile test specimen increases the stress level and significantly reduces the ductility. The reason is the positive hydrostatic stress induced by the notch, which facilitates the growth of voids. Regarding the anisotropy, the introduction of a notch reduces the difference between the stress levels in different directions (see also Fourmeau et al., 2011).

The experimental failure strains for tensile tests on notched specimens are computed in the same manner as for uniaxial tensile tests and are depicted in Fig. 6 (b). The strain to failure for the notched specimens is found less sensitive to the direction of loading than for the smooth specimens. The failure modes are illustrated in Fig. 7 (a). As pointed out by Pedersen et al. (2011), the notched specimens exhibit a cup-and-cone fracture mode and, in addition, the increased stress triaxiality caused by the notch leads to secondary cracks in the plane of the plate. The secondary cracks appear to follow the boundaries of the flat and elongated grains, and are observed in the specimens with the smallest notch radius in Fig. 7 (a) where the stress triaxiality is highest. It should be noted that contrary to smooth specimen exhibiting various failure modes, the failure mode for notched specimens is constrained by the notch geometry and remains similar for all loading directions.

3.3 *Compression tests*

For negative stress triaxialities, upsetting tests were performed on cylindrical specimens with diameter $D = 10\text{ mm}$ and height $h = 10\text{ mm}$ (see Fig. 2 (d)). The specimen axis was oriented at 0°, 45° and 90° with respect to RD. In addition, upsetting tests on specimens with loading axes along the thickness direction (ST) of the plate were conducted. The specimens were compressed between two hardened steel platens, and a graphite paste was used to lubricate the surfaces and minimize the effect of friction (Børvik et al., 2010). Five tests were performed on specimens from each of the in-plane directions, while three tests were performed on specimens sampled in the through-thickness direction (ST). Two out of five duplicate tests in the in-plane directions and all tests in the thickness direction were carried out using an extensometer attached to the platens to measure the overall deformation of the specimen. In the remaining duplicate tests in the in-plane directions, digital images of the specimens and platens were recorded with a Prosilica GC2450 digital camera equipped with a 28-105 mm Nikon lens at 10 Hz. The image series were then analysed to give the displacement of the platen on top of the specimen using an in-house 2D-DIC code (Fagerholt et al., 2010).

The Cauchy stress versus logarithmic strain curves from upsetting tests in the 0°, 45° and 90° directions in the plane and in the thickness direction (ST) of the plate are presented in Fig. 8. The Cauchy stress and logarithmic strain for these specimens are obtained by

$$\sigma = \frac{FL}{A_0 L_0}, \quad \varepsilon = \ln\left(\frac{L}{L_0}\right) \tag{3}$$

where F is the force measured by the load cell of the test machine, and L_0 and A_0 are the initial length and cross-section area of the specimen, respectively. The current length of the specimen L is determined from the displacement measurements. Since the repeatability of the tests was very good, only one representative curve is depicted in Fig. 8 for each direction of the specimens. The curves are terminated at the average failure strain obtained between parallel tests. A representative Cauchy stress-logarithmic strain curve for the tensile test in the 0° direction is also plotted (in Fig. 8) for the sake of comparison. The flow stress in the 45° loading direction is found lower than in the 0° and 90° directions, in a similar way as in the uniaxial tensile tests. However, contrary to what is observed for uniaxial tensile loading conditions, the flow stress in the 90° direction is slightly higher than in the 0° direction. In the study of Pedersen et al. (2011), it was found that the stress-strain curve from the uniaxial tension test in the 0° direction coincided with the one from the upsetting test through the thickness of the plate. This is in some conflict with the results found here, where the stress level is higher in the through-thickness upsetting test. The strain hardening is also found to be higher in the through-thickness direction (ST) than in the in-plane directions, while the strain to failure is significantly reduced. It should be kept in mind that friction can play an important role in the material response since uniaxial compression loading conditions may not be fulfilled when the plastic deformation becomes large. This will be demonstrated through numerical analysis in Section 4.

For the compression tests, fracture occurred along 45° shear planes, as shown in Fig. 9. These surfaces were flat but not always observable, since the specimen did not always split in two. The repeatability in terms of failure was compromised by friction and barrelling effects, so the specimens were arranged into different classes depending on the fracture mode. Some specimens failed abruptly across their whole height and the force dropped instantaneously to zero. In other experiments, the strain localisation occurred on the edge of the specimen, and only small force drops were observed in the measured data. Finally, some specimens did not show any drop in the stress-strain curve, although they showed multiple fracture bands spread around the rim of the sample. Such fracture modes were the case for three out of five tests in the 45° direction, and for one out of six tests in the 90° loading direction. For this latter class of specimens it was not possible to identify the strain to failure from the tests, and consequently they were not used in the computation of the average failure strain.

The average value of the strain to failure ε_f is presented in Fig. 10 as a function of the loading direction. The error bars represent the range of values obtained from duplicate tests, which is seen to be quite significant. Given the scatter between duplicate tests and the exclusion of several of the tests, no precise conclusion can be drawn with respect to the anisotropy of the strain to failure in upsetting tests in the in-plane directions. However, the strain to failure is found significantly lower in the tests in the through-thickness direction (ST) compared to the in-plane directions of loading.

3.4 *Shear tests*

To obtain stress triaxiality close to zero, shear specimens of 2 mm thickness with geometry as shown in Fig. 2 (e) were used (Gruben et al., 2011). The longitudinal axes of the spark-eroded specimens were oriented at 0°, 45° and 90° with respect to the RD. The specimens were bolted to the gripping system of the test machine to allow for possible in-plane rotations of the specimen. The force in the load cell and the displacement of the cross-head of the testing machine were continuously recorded. Owing to the spread in obtained results, 6–7 duplicate tests were performed for each direction, out of which 2–3 were instrumented for optical measurements. Before testing a fine-grained speckle pattern was spray-painted on these specimens, and the same camera and digital image correlation (DIC) analysis as for the compression tests were used, providing displacement and strain fields of the observed specimen surface. This technique is particularly relevant in these tests, since the strains were found to be inhomogeneous over the gauge sections of the specimens and eventually strain localisation occurred. One additional test was performed in the 0° direction using a high-speed camera running at a frame rate of 10 000 Hz to observe the final stage of the test. This was done in an attempt to capture the localisation of the strains leading to final failure in more detail.

Force versus displacement curves from duplicate shear tests in the 0°, 45° and 90° directions are shown in Fig. 11 (a)–(c), while representative force-displacement curves from the tests in the three directions are compared in Fig. 11 (d). Large scatter is observed in these tests. The force-displacement curves were corrected to account for the machine flexibility, but the remaining scatter in terms of force level is significant and reaches 18% of the maximum force level for the 45° loading direction. Several sources of error can be identified. A misalignment of the specimen might lead to a scatter in the plastic behaviour since the material is anisotropic. The tests were performed in two different laboratories, and some sensitivity to the different gripping systems was observed. The literature also proposes some microstructural reasons for the scatter. Rauch (1998) pointed out that shear tests in the 45° and –45° directions may show different behaviour. This possible effect was not considered in this study, since orthotropic symmetry of the material was assumed when performing the tests. Nonetheless, Fig. 11 (d), presenting the representative force-displacement curves for each direction, indicates that the ductility is somewhat lower in the 45° direction than in the 0° and 90° directions.

For the shear tests, the strain field at the surface of the specimen was determined by use of DIC. In a similar way as in the tension and compression tests, the usual effective strain is adopted here to represent failure for the shear tests. This effective strain is defined by

$$\varepsilon_{\text{eff}} = \frac{2}{\sqrt{3}}\sqrt{\varepsilon_1^2 + \varepsilon_2^2 + \varepsilon_1\varepsilon_2} \tag{4}$$

where ε_1 and ε_2 are the principal logarithmic strains in the rolling plane of the plate. The maximum strains are found along a band slightly slanted from the axis of loading, as shown in Fig. 12. The DIC analysis indicated that fracture occurs almost instantaneously along this band, since the propagation of the crack was not even captured at a frame rate of 10 000 Hz. The strain at failure ε_f is therefore defined as the average effective strain in the elements located along this band. The width of the band used for averaging was chosen equal to 0.6 mm and is represented by the arrows on Fig. 12. Fig. 10 presents the average strain to failure as a function of the loading direction, where the error bars indicate the range of values from duplicate tests. Only the results from duplicate tests instrumented for optical field measurements are included in Fig. 10. In the same manner as for the force-displacement curves, there is large scatter in measured strain to failure between duplicate tests. In this respect, it should also be kept in mind that the results depends on the width of the zone chosen for averaging the failure strain. The choice of 0.6 mm was made to take several elements into account while focusing on the area of strain localization.

In the shear tests, fracture occurred at the minimum cross-section of the specimen along a band inclined at approximately 10° with respect to the symmetry axis of the initial geometry (see Fig. 7 (b)). However, since the specimen rotated somewhat during these tests, the orientation of the surface was aligned with the direction of the loading when fracture occurred. The flat and smooth surfaces (shown for the 0° loading direction in Fig. 7 (b)) were similar in all directions of loading.

4. Numerical simulations

Non-linear finite element simulations with LS-DYNA (LSTC, 2007) were performed to accurately determine the stress and strain fields in the different tests. The numerical models of the various specimens were made with fully-integrated hexahedral solid elements (see Fig. 13). The applied constitutive relation includes isotropic elasticity, anisotropic yielding, isotropic Voce hardening and the associated flow rule. The non-quadratic anisotropic yield function Yld2004-18p proposed by Barlat et al. (2005) was adopted, and the 18 parameters were calibrated using tensile tests in seven in-plane directions and shear tests in three in-plane directions, assuming orthotropic symmetry (see Fourmeau et al., 2011, for details). The exponent m of the yield function was set equal to 12, since this value was found to give the best prediction of the experimental force-displacement curves. A friction coefficient of 0.1 was used between the lubricated platens and the cylindrical specimen loaded in compression. The simulated stress-strain curves were found to be in good agreement with the experimental results for all the tests, validating the calibrated material model from a macroscopic point of view.

To characterize the local stress and strain fields in the test specimens up to incipient failure, the spatial distribution of the accumulated plastic strain and the stress triaxiality were determined from the simulations. It should be noted that since the tests are carried out for axisymmetric specimens of different shapes as well as shear specimens, the deviatoric stress state will differ significantly from one specimen to the other. However, to limit the investigation, the stress triaxiality was selected to represent the stress state. The elements used to extract the numerical data are indicated in Fig. 13 for the various geometries. The accumulated plastic strain is defined by

$$p = \int \frac{\hat{\boldsymbol{\sigma}} : \hat{\mathbf{D}}^p}{\bar{\sigma}} \mathrm{d}t \tag{5}$$

where $\bar{\sigma}$ is the equivalent stress defined by the Yld2004-18p yield function, and $\hat{\boldsymbol{\sigma}}$ and $\hat{\mathbf{D}}^p$ are the corotational Cauchy stress and plastic rate-of-deformation tensors, respectively (see Fourmeau et al. (2011) for details). The numerical fracture point is then defined at the instant of loading where fracture occurs experimentally. It is important to note here that the accumulated plastic strain p computed from the numerical simulations is different from the strains measured experimentally and these different strain measures should not be directly compared. The stress triaxiality is here defined as

$$\sigma^* = \frac{I_1}{3\bar{\sigma}} \tag{6}$$

where $I_1 = \mathrm{tr}\left(\hat{\boldsymbol{\sigma}}\right)$ is the first invariant of the stress tensor $\hat{\boldsymbol{\sigma}}$ and plastic anisotropy is included by using the equivalent stress $\bar{\sigma}$ defined by the Yld2004-18p yield function in the definition.

To evaluate the stress and strain fields in the specimens, we consider the trajectories of accumulated plastic strain p versus stress triaxiality σ^* from incipient plastic deformation to fracture for the finite elements defining the experimentally observed failure surface (cf. Fig. 13). The envelopes of all trajectories and/or some selected trajectories are presented in the following for the different tests.

The results for the uniaxial tensile tests in the 0°, 45° and 90° directions are shown in Fig. 14. The trajectories of one of the surface elements and the element at the centre of the specimen correspond to the left and right parts of the envelope. Note that the elements considered to build the envelope depend on the loading direction and the corresponding failure mode. Thus, the elements marked in Fig. 13 (a1) are used for the 0° and 90° directions while the elements indicated in Fig. 13 (a2) are used for the 45° direction. The upper part of the envelope is defined by the experimentally observed diameter reduction at fracture, i.e. initiation of fracture in the simulations is defined by the instant in the loading process where the predicted diameter reduction is equal to the measured diameter reduction at fracture in the experiments. The trajectories displayed in Fig. 14 show that the stress triaxiality increases from the initial value at the centre of the specimen, while it slightly decreases close to the surface. This change in stress triaxiality is due to necking of the specimens, important in the 45° direction and more limited for the two other directions. The envelopes for the different directions are similar for low plastic strains, especially for the 0° and 90° directions, although the failure strain itself is quite different for these two directions. For the 45° direction the stress triaxiality at the centre of the specimen increases significantly with the accumulated plastic strain, since the large ductility in this direction allows for marked necking before fracture. The accumulated strain at failure in the finite elements representing the critical cross-section of the specimen is found rather homogeneous when failure occurs at small plastic strains ($p_f \in \left[0.156;\ 0.164\right]$ for the tensile test in the 0° direction), whereas a substantial variation is seen when the failure strain increases ($p_f \in \left[0.336;\ 0.406\right]$ for the tensile test in the 45° direction). The maximum values of the accumulated plastic strain and the stress triaxiality at failure are attained at the centre of the specimens in all three directions.

Fig. 15 presents the results for the smooth and notched specimens in the 0° direction. As explained by Fourmeau et al. (2011), the plastic flow initiates at the root of the notch and influences the stress state in the whole minimum cross-section. Since this plastic flow is anisotropic, the stress state becomes non-axisymmetric and the stress triaxiality at the centre of the minimum cross-section (at the initiation of plastic deformation) can be affected. The influence of anisotropy on the stress triaxiality is studied further in Fig. 16, which presents the envelopes for the notched specimens with $R = 2.0\,\text{mm}$ loaded in different directions. In a similar way as for tests on smooth specimens, the stress triaxiality at the centre of the minimum cross-section increases more for the 45° loading direction than for the other directions. Indeed, both the stress triaxiality and the accumulated plastic strain at failure are found to be highest for the 45° loading direction in the centre of the specimen. The accumulated plastic strains at failure are very different at the root of the notch and the centre of the minimum cross-section, giving a considerably larger strain range than under uniaxial loading conditions (e.g. in the 0° direction, $p_f \in [0.068;\ 0.127]$ for $R = 2.0\,\mathrm{mm}$ and $p_f \in [0.004;\ 0.013]$ for $R = 0.8\,\mathrm{mm}$, see Fig. 15). Fracture occurs after a very small plastic straining at the centre of the minimum cross-section (0.068 and 0.004 for notched specimens loaded in the 0° direction with $R = 2.0\,\mathrm{mm}$ and $R = 0.8\,\mathrm{mm}$, respectively), while the strain at the surface of the specimen is much larger. In some cases, the centre was not the point of maximum stress triaxiality in the minimum cross-section. This was the situation for the notched specimen with $R = 0.8\,\mathrm{mm}$, where the trajectory of the central element was actually inside the envelope (see Fig. 15). The envelope is in this case limited by the trajectory of an element located between the centre of the specimen and the root of the notch.

Another way to visualize the heterogeneities in the strain and stress fields is presented in

Fig. 17. Here the spatial distribution of the accumulated plastic strain and the stress triaxiality over the minimum cross-section is depicted for the 0° direction at the global displacement corresponding to experimental failure. For the tensile test on smooth specimens (

Fig. 17 (a)) the accumulated plastic strain and the stress triaxiality are found rather homogeneous across the section. For the tensile tests on notched specimens (

Fig. 17 (b) and (c)) the accumulated plastic strain is highest at the root of the notch, where the stress triaxiality is lowest. Further,

Fig. 17 shows that the stress and strain fields are not axisymmetric due to anisotropy, and for the notched specimen with $R = 0.8\,\mathrm{mm}$ the maximum stress triaxiality is not found at the centre of the specimen. The latter observation was also made by El-Magd et al. (1997) and Børvik et al. (2003) for steels.

The results for the compression test performed in the 0° direction are shown in Fig. 18. Fracture is assumed in the simulation when the length of the specimen corresponds to the average length at fracture in duplicate experiments. The accumulated plastic strain and the stress triaxiality in the elements forming the fracture surface are found very heterogeneous. The strong inhomogeneity in the accumulated plastic strain at fracture (e.g. $p_f \in [0.056; 0.201]$ in the through-thickness direction) makes the strains obtained from measurements of the global change in length of the specimen inaccurate and not representative for the real strains inside the specimen. Concerning the stress triaxiality, a highly compressive state of stress is found at the interface with the platen (point S2), where friction effects are important, while a uniaxial compression stress state is only ensured at mid height on the surface of the cylinder (point S1). This reveals the importance of the barrelling effect. The inclined fracture surface (see Fig. 13 (c)) contains the points with the maximum stress triaxiality. This suggests that under these negative stress triaxiality states, fracture preferentially occurs where the stress triaxiality is the highest. Note that the initial stress triaxiality is not equal to the theoretical value of –1/3 in the entire specimen due to friction effects occurring even in the elastic regime.

Fig. 19 shows the results for the shear test in the 0° direction, revealing that the specimen experiences a complex loading history that deviates somewhat from shear loading in some locations. Fracture was assumed when the central surface element reached the experimentally obtained strain to failure. The rim element S and the element I1 in Fig. 13 (d) experience stress triaxiality states deviating considerably from the theoretical value of zero. However, the elements located at the middle height of the band named I2, I3 and C experience a loading close to shear. The element at point M, which corresponds to the maximum strain location, is also shown. This point is subjected to large plastic strains, but is not located on the fracture surface and is consequently not critical. The distribution of stress triaxiality and accumulated plastic strain in the shear specimen demonstrates that the minimum cross-section is not subjected to a homogeneous shear stress. The influence of the direction of loading on the stress triaxiality field was found to be small.

5. Discussion

Uniaxial tensile tests were performed on axisymmetric smooth specimens oriented in seven in-plane directions and in the thickness direction of the plate. The numerical simulations show that both the accumulated plastic strain and the stress triaxiality reach their maximum values at the centre of the specimen. This holds for all orientations investigated numerically. The stress-strain curves given in

Fig. 3 reveal plastic anisotropy, but also that the strain to failure and the failure mode depend markedly on the direction of loading, cf. Fig. 4. Failure occurs along an inclined band for most of the orientations, but a transition to more ductile failure modes ensue as the angle between the loading and rolling direction approaches 45°. The directional variation of the fracture strain is found related to the directional variation of the strain ratio, i.e. a low strain ratio implies low ductility and vice versa. Since a low strain ratio indicates a reduced thinning resistance of the plate during stretching, the low ductility occurs in orientations where the plastic deformation results in substantial thinning of the plate. Similar failure mode transition as described above has been observed for the AA5083-H116 aluminium alloy, which exhibits the Portevin-Le Chatelier (PLC) effect for some ranges of strain rate and temperature (Clausen et al., 2004). For AA5083 the transition is observed for pure uniaxial tension if the strain rate is moved from a zone where no PLC effect is seen to a zone where PLC effect is observed. The underlying softening mechanism behind the localization (and transition) process is believed to be the strain rate sensitivity that is negative in the PLC regime and turns positive when no PLC is present. For the AA7075 material studied here, no such softening mechanism is apparently present. However, a possible explanation for the shear failure is a geometrical softening due to texture evolution, which would be different for the different loading directions. The crystallographic texture, the flat and elongated grains, the particle distribution and the PFZs will also influence the shear localization taking place in some loading directions. The specimens tested in the thickness direction of the plate all exhibited fracture along the elongated and flat grains in the rolling plane. It is likely that fracture occurs in the soft PFZs adjacent to the grain boundaries (see Fig. 5). The ductility in this direction was significantly lower than in any of the in-plane directions.

Tensile tests were performed on notched axisymmetric specimen with notch root radii $R = 2.0\ \mathrm{mm}$ and $R = 0.8\ \mathrm{mm}$ in the 0°, 45° and 90° directions. Failure occurred at the minimum cross-section in a cup-and-cone failure mode in all cases. This result may be influenced by the geometry of the specimen not allowing shear failure along an inclined fracture surface. Secondary cracks along the flat and elongated grains in the rolling plane were observed because of the high level of stress triaxiality induced by the notch. As remarked by Pedersen et al. (2011), the regions in the neighbourhood of the grain boundaries are weak areas owing to the precipitate free zones and the grain boundary particles. The stress-strain curves and strain to failure reveal that plastic anisotropy has less influence on the global behaviour of the notched specimen than of the smooth specimens (see Fig. 6). However, the distribution of stress triaxiality and accumulated plastic strain over the minimum cross-section of the notch depends on the loading direction (see Fig. 16). As explained by Fourmeau et al. (2011), the anisotropic plastic behaviour makes the stress state non-axisymmetric. For the notched specimens, the location of the maximum stress triaxiality is not always at the centre of the minimum cross-section, and the plastic strain may be highest at the surface (see

Fig. 17). This makes it difficult to determine the exact location of fracture initiation. In addition, the possibility of internal initiation of failure may lead to a non-conservative value of the strain to failure.

Compression tests were performed on cylinders with aspect ratio $h/D = 1$ in the 0°, 45° and 90° directions with respect to the rolling (RD) and in the thickness (ST) directions of the plate. Failure occurred along localized 45° bands in a similar way as for the uniaxial tensile tests on smooth specimens exhibiting shear failure. The stress and strain fields in the numerical simulations were highly inhomogeneous, the stress triaxiality was far from the theoretical value of –1/3 and the local strains deviated markedly from the global logarithmic strain after barrelling. However, the simulations revealed that the failure surfaces found experimentally correspond to planes where the stress triaxiality reaches a maximum (positive values in some cases). These heterogeneities caused by the barrelling of the specimen may also explain the large scatter between duplicate tests in terms of strain to failure. Consequently, no quantitative conclusion on the anisotropy of strain to failure can be drawn, except the much lower value observed in the through-thickness direction (ST), as presented in Fig. 10. This is consistent with the low strain to failure found for uniaxial tension in this direction and shows that the ductility in the through-thickness direction is generally markedly lower than the ductility in the in-plane directions.

Shear tests were performed on butterfly specimens in the 0°, 45° and 90° directions with respect to the rolling direction of the plate. Failure occurred at the minimum cross-section along a flat surface. Both the force-displacement curves (Fig. 11) and the DIC analyses (Fig. 10) indicate lower ductility in the 45° loading direction. Numerical simulations of the shear tests show that both stress triaxiality and accumulated plastic strain are inhomogeneous along the fracture surface. Only the central part of the shear zone is submitted to shear loading. This makes it difficult to determine the location of fracture initiation from the numerical simulations, but the DIC analyses indicate that fracture occurs almost instantaneously along the entire deformation zone. Large scatter was observed in the force-displacement curves and the strain to failure between duplicate tests, and the results for the shear tests should be considered only in a qualitative way.

For both uniaxial tensile and compression tests in which shear failure occurred, the fracture surfaces were oriented at 45° with respect to the loading direction, but not in a random manner. Let us assume that the minimum cross-section of the specimen has an elliptic shape. Two possible orientations (among infinitely many) of the fracture surface with respect to the loading axis were observed. The fracture surface was oriented at 45° to the loading direction and contained either the semi-major axis or the semi-minor axis of the ellipse. Observations of the various fracture surfaces revealed that the latter case occurred consistently in uniaxial tension and preferentially in compression. Since the oval shape of the cross-section is defined by the plastic anisotropy, this observation suggests that the localization process is intimately related to the strain ratio. The strain ratios for the uniaxial compression tests are not presented since no continuous measurement of the diameter was performed during these tests. However, the elliptical fractured specimens for compression tests suggest that the strain ratios are similar in uniaxial tension and compression.

It is usual to present the fracture locus for a material where the strain to failure is given as a function of the stress triaxiality (e.g. Bao and Wierzbicki, 2004). Recently, the importance of the Lode parameter has been discussed (e.g. Zhang et al., 2001; Nahshon and Hutchinson, 2008; Bai and Wierzbicki, 2008; Barsoum and Faleskog, 2011), and it is then necessary to construct a fracture surface where the strain to failure is plotted as a function of stress triaxiality and Lode parameter. The fracture surface should present the local fracture strain versus the local values of stress triaxiality and Lode parameters at the location where failure initiates in the specimen. Based on experiments, the local values of stress and strain and the location of failure are often difficult to determine accurately and numerical simulations are required for this purpose. In addition, the construction of a failure surface rests on the assumption of proportional straining up to failure. Recently, the effect of loading path on the fracture locus was examined theoretically by means of an axisymmetric void cell model by Benzerga et al. (2012). They found that under non-radial loadings, an infinite number of fracture loci in terms of a failure strain versus average stress triaxiality and Lode parameter can be constructed. Thus, they claimed that the notion of a “fracture locus” is a misnomer. Based on the experimental and numerical results from the present study it is not possible to establish a valid fracture locus, since the stress state varies during straining and the location of failure initiation is not known due to the heterogeneous stress and strain fields. Instead, the “global” strains to failure obtained from the various tests are compared in Fig. 20 where the tests are ordered after increasing “global” stress triaxiality. The complex variation of the strain to failure with loading direction and specimen type is apparent in this figure, but an overall trend of a decreasing global strain to failure with increasing global stress triaxiality is found. The exceptions are the low ductility found in compression through the thickness of the plate and the high ductility in uniaxial tension in the 45° loading direction.

The AA7075-T651 alloy exhibits a complex microstructure including crystallographic texture, flat and elongated grains, stringers of constituent particles in the rolling plane and PFZs with grain boundary precipitation (Pedersen et al., 2011). The results with respect to the mechanical properties are considerable anisotropy with respect to strength, plastic flow and ductility. Regarding the variation of ductility with loading direction and stress state, it is supposed that the distribution of the constituent particles and the PFZs are important, but also the directionality of the plastic flow has been shown to influence the ductility. Owing to the complex variation of the strain to failure with loading direction and stress state, it seems required to develop constitutive models representing in some way these microstructural features, but due to the small scale and complex distribution of the constituent particles and the PFZs, this is a very challenging task

6. Conclusions

From this study, the following main conclusions can be drawn:

- In in-plane uniaxial tension, the strain to failure varies strongly with the loading direction, in a similar way as the strain ratio. The ductility is low for low values of the strain ratio and vice versa. Failure occurs in a cup-and-cone mode in the directions with the highest ductility and in a shear mode in the directions with lowest ductility.
- The strain to failure for the notched tensile specimens is markedly reduced compared with the smooth specimens due to the increased levels of stress triaxiality. The fracture occurs in a cup-and-cone mode in all orientations and secondary cracks in the rolling plane are observed. The directional variation of the strain to failure is moderate.
- In the in-plane upsetting tests, the failure occurred along 45° shear planes. The variation in strain to failure with direction was moderate, but due to the lower stress triaxiality, strain to failure was consistently higher than in the corresponding uniaxial tension test. The numerical simulations indicate that the fracture occurs along planes where the stress triaxiality reaches its maximum level.
- In the shear tests, the failure surface was flat and aligned with the direction of loading, and the DIC analysis indicated that fracture occurs almost instantaneously along the entire gauge length. The direction dependency of the strain to failure was moderate, but the results are compromised by the large scatter between duplicate tests. The finite element simulations demonstrated that only the middle part of the gauge section was subjected to pre-dominant shear loading, while close to the edges, complex, non-radial loadings were observed.

- The tensile and compression tests in the through-thickness direction of the plate exhibit low ductility, and the average strain to failure is similar, even if the “global” stress triaxiality is very different. In the tension tests, the failure occurs in the rolling plane along the flat and elongated grain boundaries where precipitate free zones are located. The scatter is large, probably due to the small dimensions of the specimen compared to the grain size. In compression, failure occurs in a shear mode with a fracture surface inclined 45° to the loading axis.
- Owing to the plastic anisotropy, the cross section of the uniaxial tension and compression specimens deformed into an elliptic shape. In the cases where failure occurred in a shear mode, the orientation of the fracture surface was 45° with the loading axis and contained either the semi-major axis or the semi-minor axis of the ellipse.
- The finite element simulations show that the stress and strain fields are heterogeneous over the critical cross-section of the specimens. It is difficult to determine the location of fracture initiation and, accordingly, it is not possible to determine the failure strain and its relation to the stress state.

Acknowledgements

The financial support of this work from the Structural Impact Laboratory (SIMLab), Centre for Research-based Innovation (CRI) at the Norwegian University of Science and Technology (NTNU), is gratefully acknowledged. The authors would also like to aknowledge Dr. Torodd Berstad for help with the numerical simulations and Dr. Ketill O. Pedersen for the assistence with the metallurgical study.

References

Andreatta, F., Terryn, H., De Wit, J.H.W., 2003. Effect of solution heat treatment on galvanic coupling between intermetallics and matrix in AA7075-T6. Corros. Sci. 45, 1733-1746.

Bai, Y., Wierzbicki, T., 2008. A new model of metal plasticity and fracture with pressure and Lode dependence. Int. J. Plasticity 24, 1071-1096.

Bai, Y., Wierzbicki, T., 2010. Application of extended Mohr–Coulomb criterion to ductile fracture. Int. J. Fracture 161, 1-20.

Bao, Y., Wierzbicki, T., 2004. On fracture locus in the equivalent strain and stress triaxiality space. Int. J. Mech. Sci. 46, 81-98.

Barlat, F., Aretz, H., Yoon, J.W., Karabin, M.E., Brem, J.C., Dick, R.E., 2005. Linear transfomation-based anisotropic yield functions. Int. J. Plasticity 21, 1009-1039.

Barsoum, I., Faleskog, J., 2007. Rupture mechanisms in combined tension and shear - experiments. Int. J. Solids Struct. 44, 1768-1786.

Barsoum, I., Faleskog, J., 2011. Micromechanical analysis on the influence of the Lode parameter on void growth and coalescence, Int. J. Solids Struct. 48, 925-938.

Benzerga, A., Surovik, D., Keralavarma, S.M., 2012. On the path-dependence of the fracture locus in ductile materials – Analysis. Int. J. Plasticity 37, 157-170.

Børvik, T., Hopperstad, O.S., Berstad, T., 2003. On the influence of stress triaxiality and strain rate on the behaviour of a structural steel. Part II. Numerical study. Euro. J. Mech. A-Solid 22, 15-32.

Børvik, T., Hopperstad, O. S., Pedersen, K. O., 2010. Quasi-brittle fracture during structural impact of AA7075-T651 aluminium plates. Int. J. Impact Eng. 37, 537-551.

Chen, Y., Pedersen, K.O., Clausen, A.H., Hopperstad, O.S., 2009. An experimental study on the dynamic fracture of extruded AA6xxx and AA7xxx aluminium alloys. Mater. Sci. Eng. A-Struc. 523, 253-262.

Chu, C. C., Needleman, A., 1980. Void nucleation effects in biaxially stretched sheets. ASME J. Eng. Mater. Technol. 102, 249-256.

Clausen, A.H., Børvik, T., Hopperstad, O.S., Benallal, A., 2004. Flow and fracture characteristics of aluminium alloy AA50832009. An experimental study on the dynamic fracture of extrud. Mater. Sci. Eng. A-Struct. 364, 260-272.

Dumont, D., Deschamps, A., Brechet, Y., 2003. On the relationship between microstructure, strength and toughness in AA7075 aluminium alloy. Mat. Sci. Eng. A-Struct 356, 326-336.

Dunand, M. and Mohr, D., 2011. On the predictive capabilities of the shear modified Gurson and the modified Mohr-Coulomb fracture models over a wide range of stress triaxialities and Lode angles. J. Mech. Phys. Solids 59, 1374-1394.

El-Magd, E., 1997. Influence of strain rate on ductility of metallic materials. Steel Res. 68, 67-71.

Fagerholt, E., Dørum, C., Børvik, T., Laukli, H.I., Hopperstad, O.S., 2010. Experimental and numerical investigation of fracture in a cast aluminium alloy. Int. J. Solids Struct. 47, 3352-3365.

Fourmeau, M., Børvik, T., Benallal, A., Lademo, O.G., Hopperstad, O.S., 2011. On the plastic anisotropy of an aluminium alloy and its influence on constrained multiaxial flow. Int. J. Plasticity 27, 2005-2025. Special Issue In Honor of Nobutada Ohno.

Gologanu, M., Leblond, J.B., Devaux, J., 1993. Approximate models for ductile metals containing nonspherical voids — case of axisymmetric prolate ellipsoidal cavities. J. Mech. Phys. Solids 41, 1723-1754.

Gologanu, M., Leblond, J.-B., Devaux, J., 1994. Approximate models for ductile metals containing nonspherical voids — case of axisymmetric oblate ellipsoidal cavities. ASME J. Eng. Mater. Technol. 116, 290-297.

Gologanu, M., Leblond, J.-B., Devaux, J., 1994. Numerical and theoretical study of coalescence of cavities in periodically voided solids. ASME Comp. Mater. Model. 42, 223-244.

Gruben, G., Fagerholt, E., Hopperstad, O.S., Børvik, T., 2011. Fracture characteristics of a cold-rolled dual-phase steel. Eur. J. Mech. A-Solid, 30, 204-218.

Gurson, A.L., 1977. Continuum theory of ductile rupture by void nucleation and growth. Part I : yield criteria and flow rules for porous ductile media. ASME J. Eng. Mater. Technol. 99, 2-15.

Hahn, G., Rosenfield, A., 1975. Metallurgical factors affecting fracture toughness of aluminum alloys. Metall. Mater. Trans. A 6, 653-668.

Hill, R., 1948. A theory of the yielding and plastic flow of anisotropic metals. Proc. R. Soc. Lond. A 193, 281-297.

Jordon, J. B., Horstemeyer, M. F., Solanki, K., Bernard, J. D., J.T. Berry, J. T., Williams, T. N., 2009. Damage characterization and modeling of a 7075-T651 aluminum plate. Mater. Sci. Eng. A-Struct. 527, 169-178.

Khan, A.S., Liu, H., 2012. A new approach for ductile fracture prediction on Al 2024-T351 alloy. Int. J. Plasticity 35, 1-12.

Lecarme, L., Tekoglu, C., Pardoen, T., 2011. Void growth and coalescence in ductile solids with stage III and stage IV strain hardening. Int. J. Plasticity 27, 1203-1223.

LSTC, LS-DYNA Keyword User’s Manual, Version 971, 2007. Livermore Software Technology Corporation, California.

Luo, M., Dunand, M., Mohr, D., 2012. Experiments and modelling of anisotropic aluminium extrusions under multi-axial loading-Part II: Ductile fracture. Int. J. Plasticity 32-33, 36-58.

McClintock, F.A., 1968. A criterion for ductile fracture by the growth of holes. J. Appl. Mech. 35, 363-371.

Nahshon, K., Hutchinson, J.W., 2008. Modification of the Gurson Model for shear failure, Euro. J. Mech. A-Solids 27, 1-17.

Pardoen, T., Hutchinson, J.W., 2000. An extended model for void growth and coalescence. J. Mech. Phys. Solids 48, 2467-2512.

Park, J.K., Ardell, A.J., 1988. Precipitate microstructure of peak-aged 7075 al. Scripta Metall. 22, 1115-1119.

Pedersen, K.O., Børvik, T., Hopperstad, O.S., 2011. Fracture mechanisms of aluminium alloy AA7075-T651 under various loading conditions. Mater. Design 32, 97-107.

Rauch, E.F., 1998. Plastic anisotropy of sheet metals determined by simple shear tests. Mater. Sci. Eng. A-Struct. 241, 179-183.

Rice, J.R., Tracey, D.M., 1969. On the ductile enlargement of voids in triaxial stress fields. J. Mech. Phys. Solids 17, 201-217.

Rousselier, G., Luo, M., Mohr, D., 2012. Macroscopic plasticity modeling of anisotropic aluminum extrusions using a Reduced Texture Methodology. Int. J. Plasticity 30-31, 144-165.

Steglich, D., Brocks, W., Heerens, J., Pardoen, T., 2008. Anisotropic ductile fracture of al 2024 alloys. Eng. Fract. Mech. 75, 3692-3706. Microstructurally Aided Fracture Mechanisms.

Stoughton, T.B., Yoon, J.W., 2011. A new approach for failure criterion for sheet metals. Int. J. Plasticity 27, 440-459.

Teirlinck, D., Zok, F., Embury, J.D., Ashby, M.F., 1988. Fracture mechanism maps in stress space. Acta Metall. 36, 1213-1228.

Thomason, P.F., 1990. Ductile Fracture of Metals. Oxford, Pergamon Press.

Tvergaad, V., Needleman, A., 1984. Analysis of the cup-cone fracture in a round tensile bar. Acta Metall. 32, 157-169.

Yerra, S. K., Tekoglu, C., Sheyvaerts, F., Delannay, L., Van Houtte, P., Pardoen, T., 2010. Void growth and coalescence in single crystals. Int. J. Solids Struct. 47, 1016-1029.

Wierzbicki, T., Bao, Y., Lee, Y.W., Bai, Y., 2005. Calibration and evaluation of seven fracture models. Int. J. Mech. Sci. 47, 719-743.

Zhang, K.S., Bai, J.B., François, D., 2001. Numerical analysis of the influence of the Lode parameter on void growth, Int. J. Solids Struct. 38, 5847-5856.

Table caption

Table 1. Chemical composition (in weight %) of the aluminium alloy AA7075-T651.

Figure captions

Fig. 1. Tri-planar optical micrographs showing (a) the grain structure and (b) the distribution of constituent particles for the AA7075-T651 aluminium alloy (Børvik et al., 2010).

Fig. 2. Specimen geometries: (a) smooth tension tests in the rolling plane, (b) smooth tension tests in the thickness direction (ST), (c) notched tension tests in the rolling plane, (d) upsetting tests with aspect ratio $h/D = 1$ and (e) shear tests in the rolling plane.

Fig. 3. Cauchy stress versus logarithmic strain in uniaxial tension from (a) representative tests in the rolling plane at 0°, 15°, 30°, 45°, 60°, 75° and 90° with respect to the rolling direction (RD) and (b) duplicate tests in the thickness direction (ST) of the plate. In (a), the curves are plotted up to the average strain to failure.

Fig. 4. Uniaxial tension tests in the rolling plane and through the thickness of the plate. (a) Average values of the experimental failure strain and strain ratio versus loading direction with error bars representing the range of values obtained in parallel tests. (b) Failure modes where the labels at the top and bottom give the orientation angle and the failure strain, respectively.

Fig. 5. High magnification optical micrograph of longitudinal mid-section at the fracture location in a tensile test on a smooth axisymmetric specimen loaded in the through-thickness direction of the plate (ST).

Fig. 6. Tension tests on smooth and notched specimens in the rolling plane of the plate: (a) Cauchy stress versus logarithmic strain for representative tests at 0°, 45° and 90° with respect

to the rolling direction (RD) of the plate. The curves are plotted up to the average strain to failure for each direction and notch radius. (b) Average values of the experimental strain to failure versus loading direction with error bars representing the range of values obtained in parallel tests.

Fig. 7. Failure modes observed in the 0° loading direction for (a) notched tension specimens with different notch radii (Pedersen et al., 2011) and (b) butterfly specimen used in the shear tests.

Fig. 8. Representative Cauchy stress versus logarithmic strain for the compression tests on cylindrical specimens aligned at 0°, 45° and 90° with respect to the rolling direction (RD) and with the thickness direction (ST) of the plate. Result for the uniaxial tension test performed in the 0° direction is also shown for the sake of comparison.

Fig. 9. Failure modes for the compression tests aligned at (a) 0°, (b) 45°**,** (c) 90° with respect to the rolling direction (RD) and (d) with the thickness direction (ST) of the plate. The line depicted on the top of the specimen in (a), (b) and (c) represents the thickness direction of the plate.

Fig. 10. Average values of the experimental strain to failure versus loading direction with respect to RD for compression and shear tests in the rolling plane of the plate. The results for the compression test in the thickness direction (ST) are also shown. The error bars represent the range of values obtained in parallel tests. Note that the compression tests not showing clear fracture and the shear tests not instrumented for optical field measurements were excluded from this diagram.

Fig. 11. Force versus global displacement for the shear tests on butterfly specimens aligned at (a) 0°, (b) 45° and (c) 90° with respect to the rolling direction (RD) of the plate. In (d), representative force-displacement curves for the three directions of loading are compared.

Fig. 12. Effective strain field obtained by digital image correlation from the last image before fracture for a shear test in the 45° direction with respect to RD.

Fig. 13. Finite element meshes of the test specimens. The elements in black show where fracture is assumed to occur for (a) tensile tests on smooth specimen (the different cases (a1) and (a2) correspond to different failure modes), (b) tensile tests on notched specimen of $R = 2.0\ \mathrm{mm}$, (c) upsetting tests on cylinders with $h/D = 1.0$ and (d) shear tests on butterfly specimens.

Fig. 14. Envelopes of the trajectories of accumulated plastic strain versus stress triaxiality for uniaxial tension tests. The results are taken from the elements depicted in black in Fig. 13 (a1) for the 0° and 90° directions and in Fig. 13 (a2) for the 45° direction. The trajectories for the surface element and the element in the centre of the specimen represent the left and right boundaries of the envelopes after necking. All other trajectories are comprised between these lines and are terminated at the diameter reduction corresponding to failure in the experiments.

Fig. 15. Envelopes of the trajectories of accumulated plastic strain versus stress triaxiality for uniaxial and notched tensile tests in the rolling direction (RD) of the plate. The results are taken from the elements depicted in black in Fig. 13 (a1) and (b). The trajectories for the surface element, giving the minimum stress triaxiality, and the element in the centre of the specimen, not always giving the highest stress triaxiality, are shown. All trajectories are terminated at the diameter reduction corresponding to failure in the experiments.

Fig. 16. Envelopes of the trajectories of accumulated plastic strain versus stress triaxiality for the notched tensile tests with $R = 2\ \mathrm{mm}$ performed in the 0°, 45° and 90° directions. The results are taken from the elements depicted in black in Fig. 13 (b). The trajectories for the surface element and the element in the centre of the specimen represent the left and right boundaries of the envelopes. All other trajectories are comprised between these lines and are terminated at the diameter reduction corresponding to failure in the experiments.

Fig. 17. The distributions of accumulated plastic strain and stress triaxiality over the minimum cross-section for tensile tests in the 0° direction with respect to the rolling direction for (a) smooth specimen, (b) notched specimen with notch radius $R = 2.0\ \mathrm{mm}$ and (c) notch specimens with notch radius $R = 0.8\ \mathrm{mm}$.

Fig. 18. Trajectories of accumulated plastic strain versus stress triaxiality for the compression tests on cylinders with $h/D = 1$ loaded in the rolling direction (RD) of the plate. The results are

from the elements depicted in black in Fig. 13 (c). Note that the trajectories for the points C, S1 and S3 are close to uniaxial compressive loading, whereas the trajectory for the point S2 reveals a multi-axial compressive loading. All trajectories are terminated at the displacement corresponding to failure in the experiment.

Fig. 19. Trajectories of accumulated plastic strain versus stress triaxiality for the shear test in the rolling direction (RD) of the plate. Results are taken from the elements depicted in black in Fig. 13 (d). Note that the trajectories from the points C, I2 and I3 are close to a shear loading whereas those for I1 and S are not. The stress triaxiality in point M, corresponding to the maximum strain location, deviates somewhat from shear loading. All trajectories are terminated when the strain in the central surface element corresponds to the failure strain determined in the DIC analysis.

Fig. 20. Comparison of the experimental strain to failure for the compression tests (CT), shear tests (ST), uniaxial tension tests (UT), notched tension tests with 2.0 mm radius (NT2.0) and notched tension tests with 0.8 mm radius (NT0.8). The average value is plotted with the error bars representing the range of values obtained in parallel tests.

Figure 1

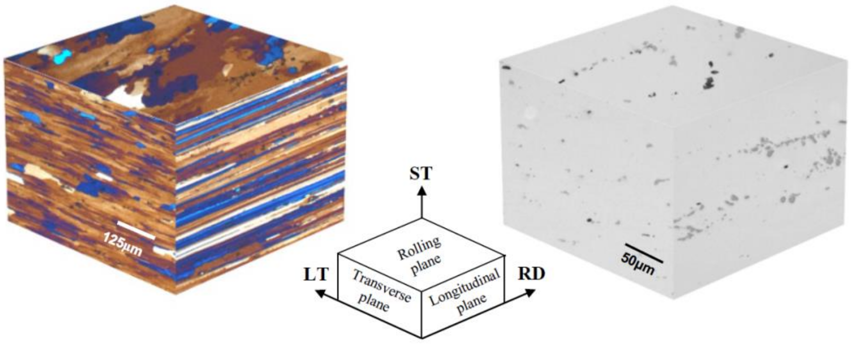
125µm
ST
Rolling plane
LT
Transverse plane
Longitudinal plane
RD
50µm

(a) (b)

Figure 2

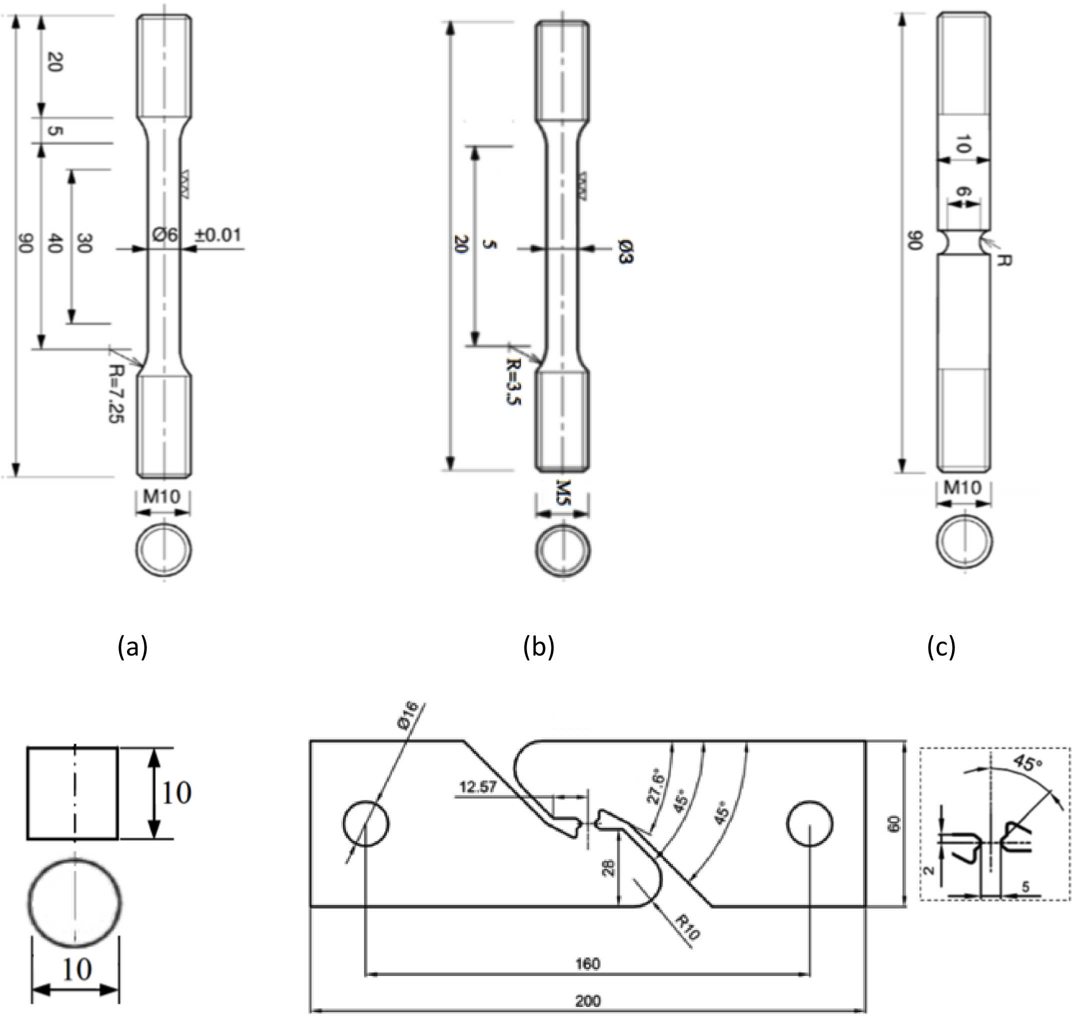

(a) (b) (c)

(d) (e)

Figure 3

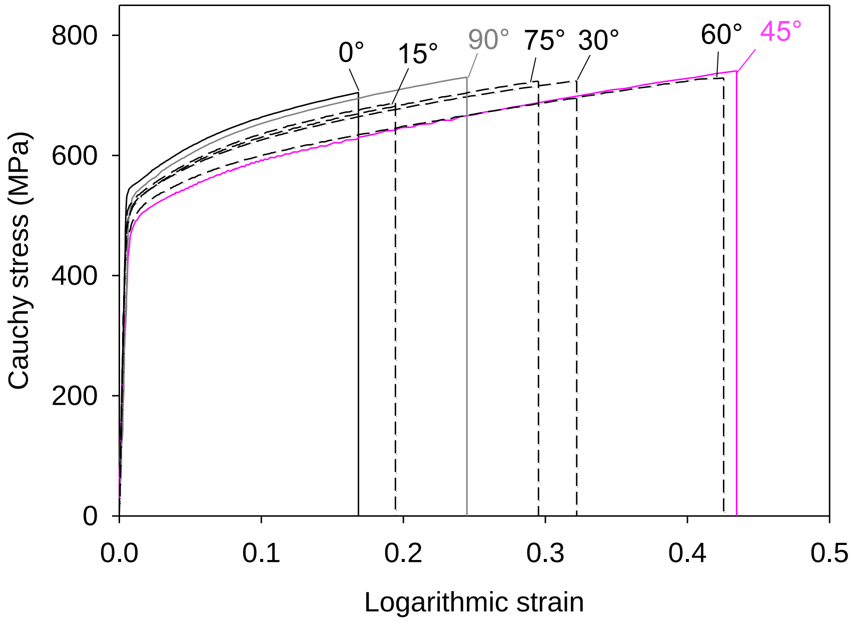
0°
15°
90°
75°
30°
60°
45°
800
600
400
200
0
Cauchy stress (MPa)
0.0
0.1
0.2
0.3
0.4
0.5
Logarithmic strain

(a)

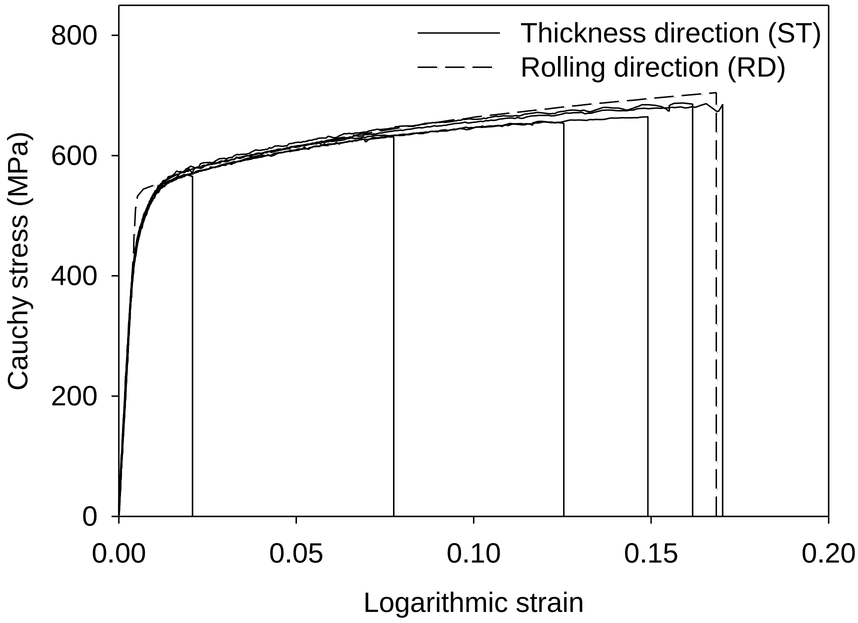
Thickness direction (ST)
Rolling direction (RD)
800
600
400
200
0
Cauchy stress (MPa)
0.00
0.05
0.10
0.15
0.20
Logarithmic strain

(b)

Figure 4

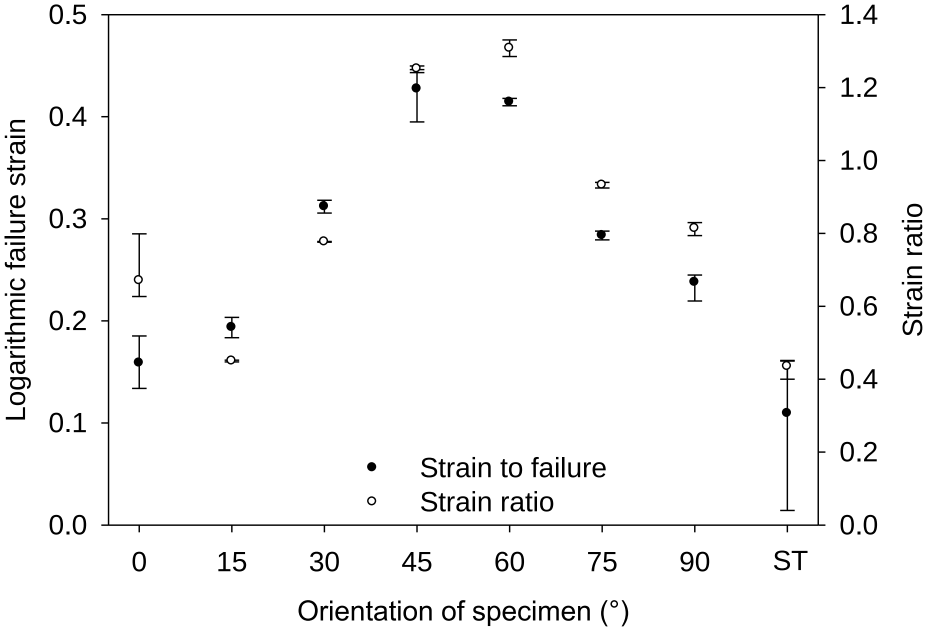

0.5
0.4
0.3
0.2
0.1
0.0
Logarithmic failure strain
1.4
1.2
1.0
0.8
0.6
0.4
0.2
0.0
Strain ratio
● Strain to failure
○ Strain ratio
0
15
30
45
60
75
90
ST
Orientation of specimen (°)

(a)

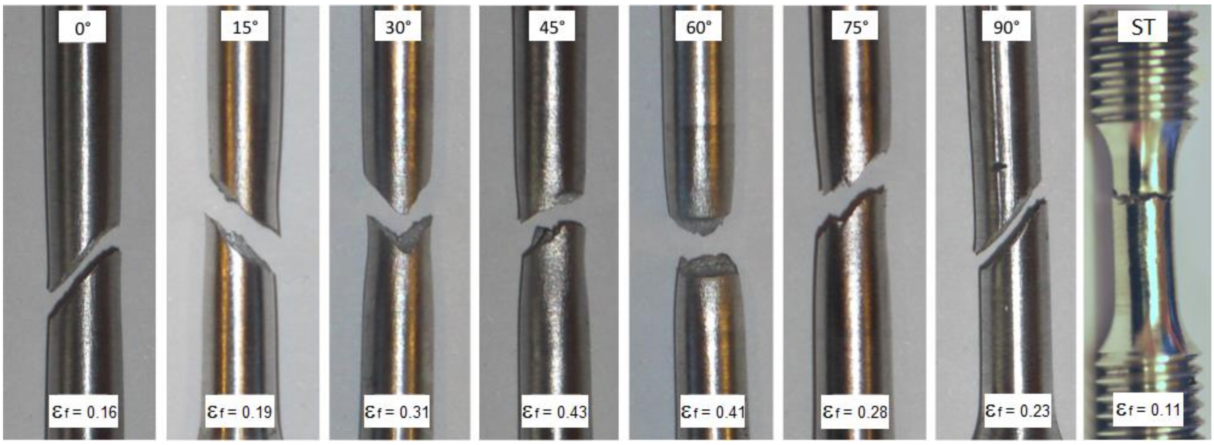

0°
$\varepsilon_f = 0.16$
15°
$\varepsilon_f = 0.19$
30°
$\varepsilon_f = 0.31$
45°
$\varepsilon_f = 0.43$
60°
$\varepsilon_f = 0.41$
75°
$\varepsilon_f = 0.28$
90°
$\varepsilon_f = 0.23$
ST
$\varepsilon_f = 0.11$

(b)

Figure 5

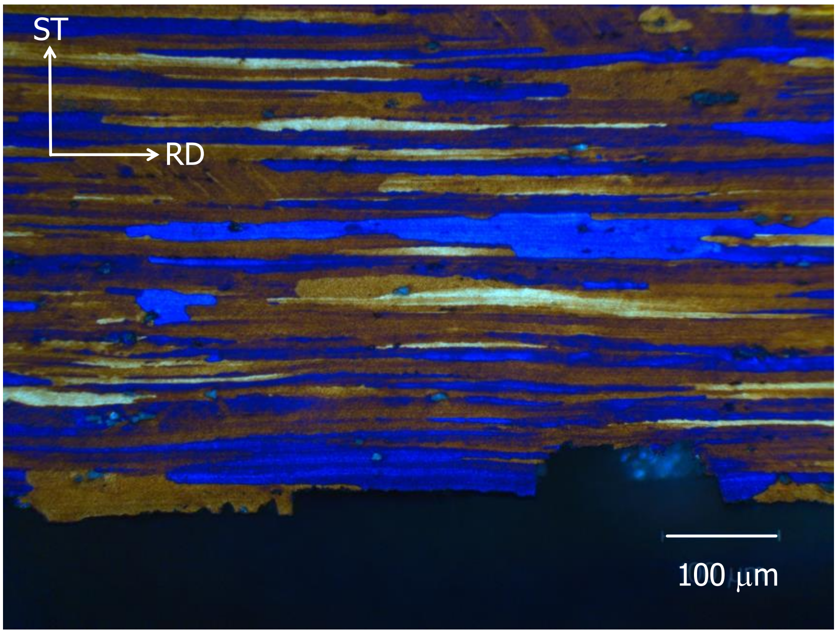

Figure 6

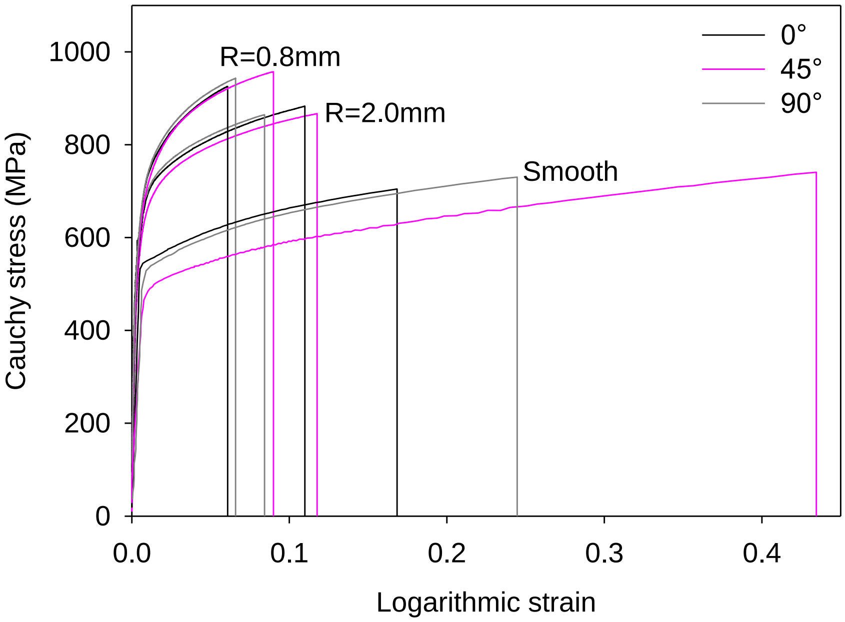

Cauchy stress (MPa)
1000
800
600
400
200
0
0.0
0.1
0.2
0.3
0.4
Logarithmic strain
R=0.8mm
R=2.0mm
Smooth
0°
45°
90°

(a)

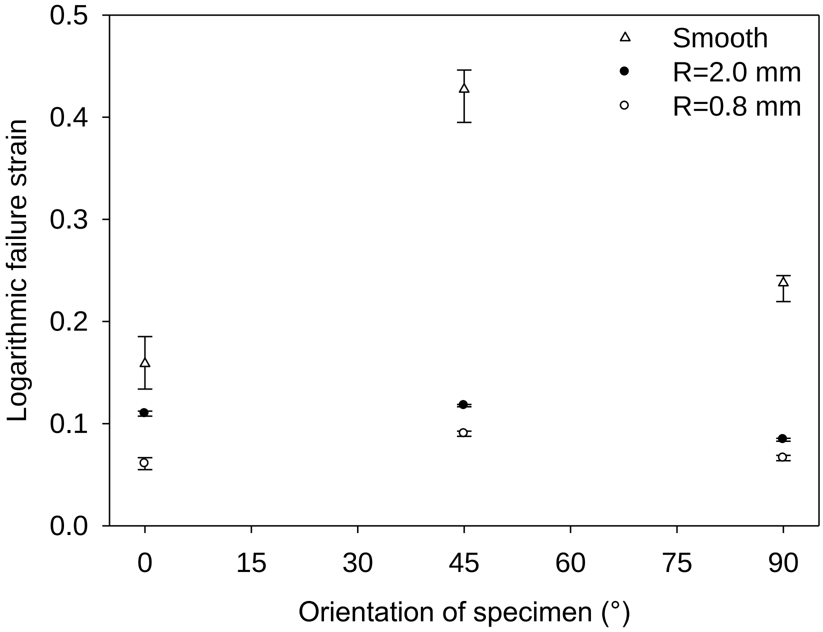

Logarithmic failure strain
0.5
0.4
0.3
0.2
0.1
0.0
0
15
30
45
60
75
90
Orientation of specimen (°)
Smooth
R=2.0 mm
R=0.8 mm

(b)

Figure 7

(a) (b)

Figure 8

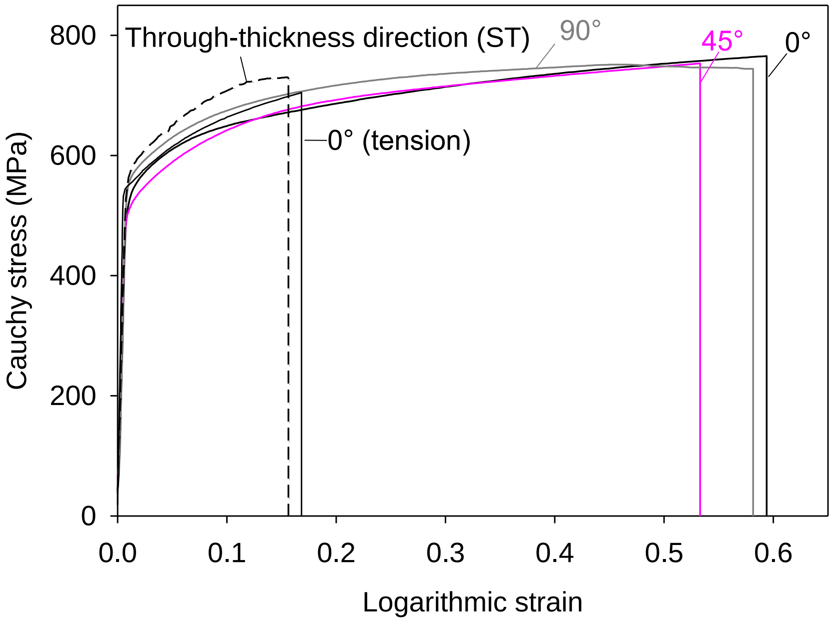

Through-thickness direction (ST)
90°
45°
0°
0° (tension)
Cauchy stress (MPa)
800
600
400
200
0
0.0
0.1
0.2
0.3
0.4
0.5
0.6
Logarithmic strain

Figure 9

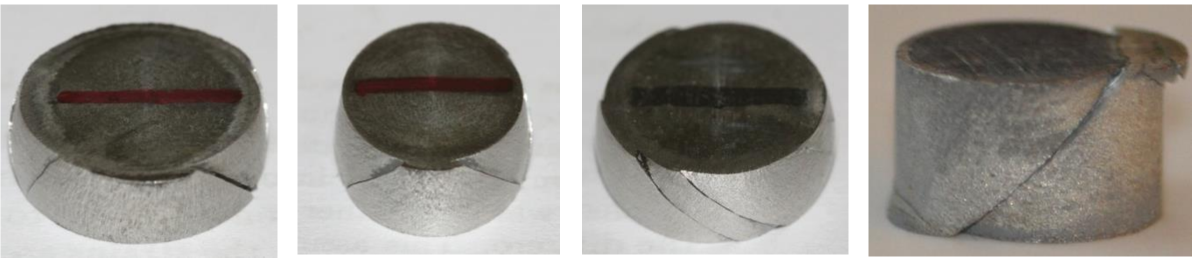

(a) (b) (c) (d)

Figure 10

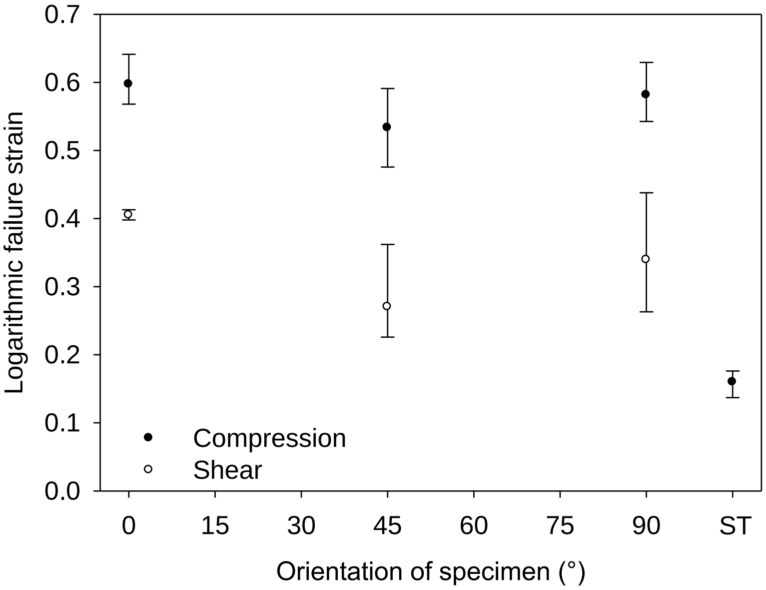
0.7
0.6
0.5
0.4
0.3
0.2
0.1
0.0
Logarithmic failure strain
● Compression
○ Shear
0
15
30
45
60
75
90
ST
Orientation of specimen (°)

Figure 11

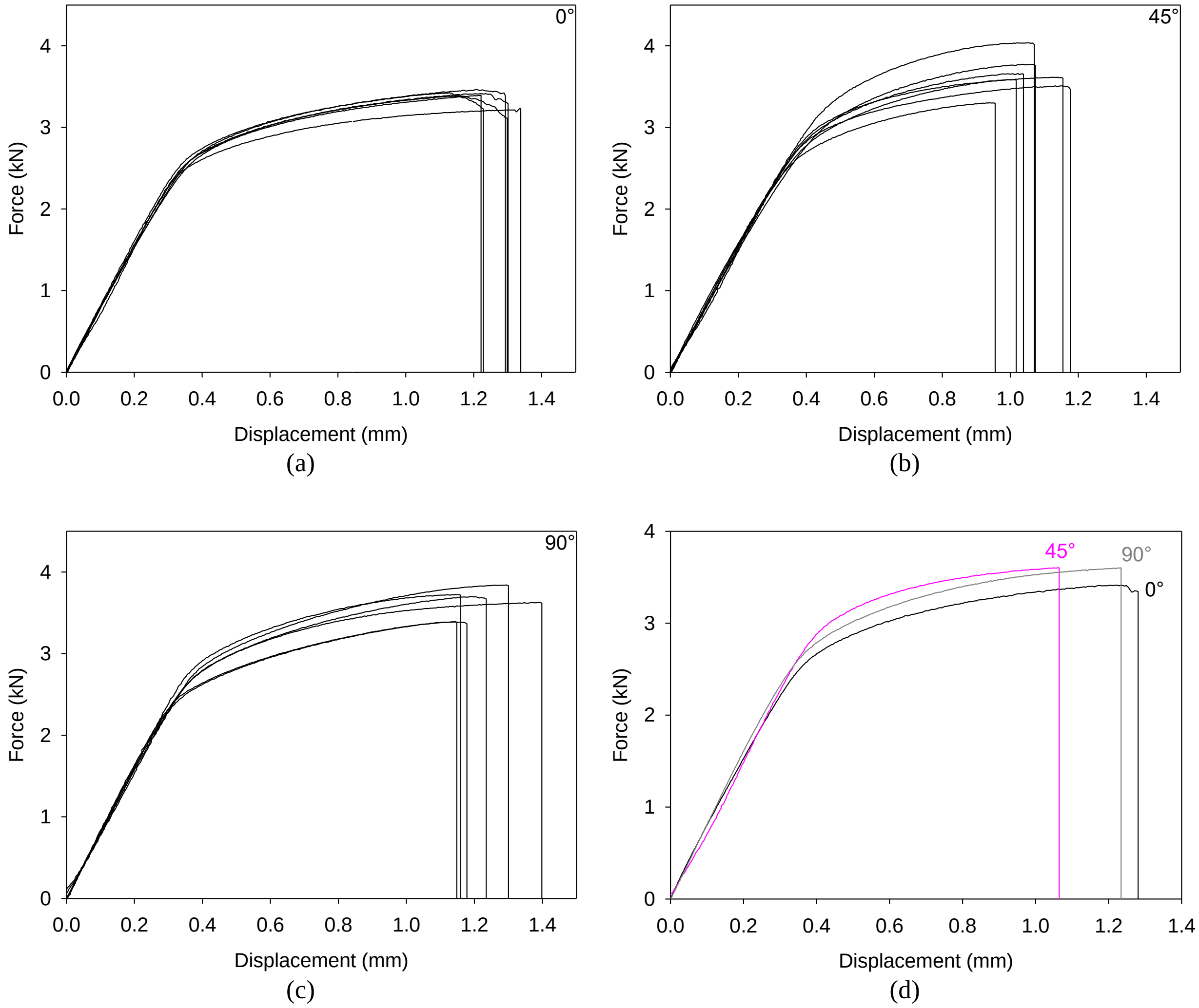

(a) (b) (c) (d)

Figure 12

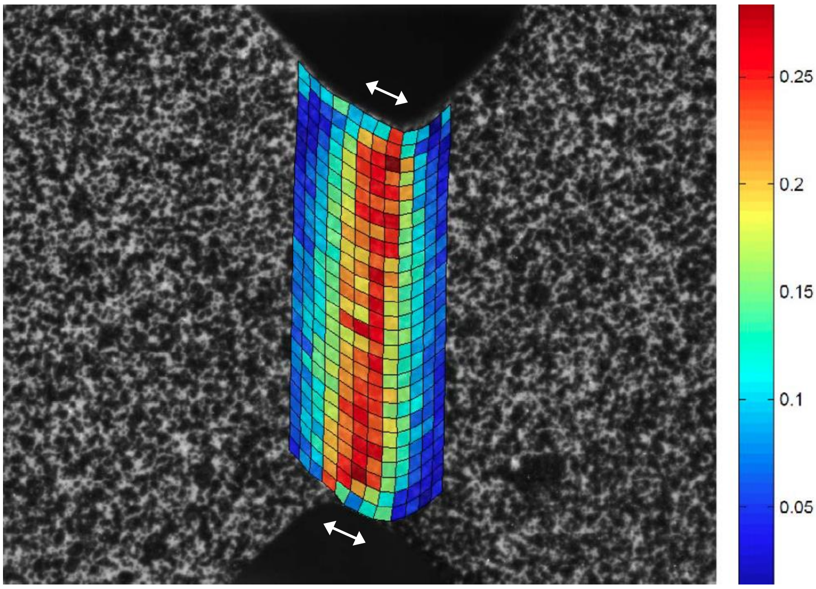

Figure 13

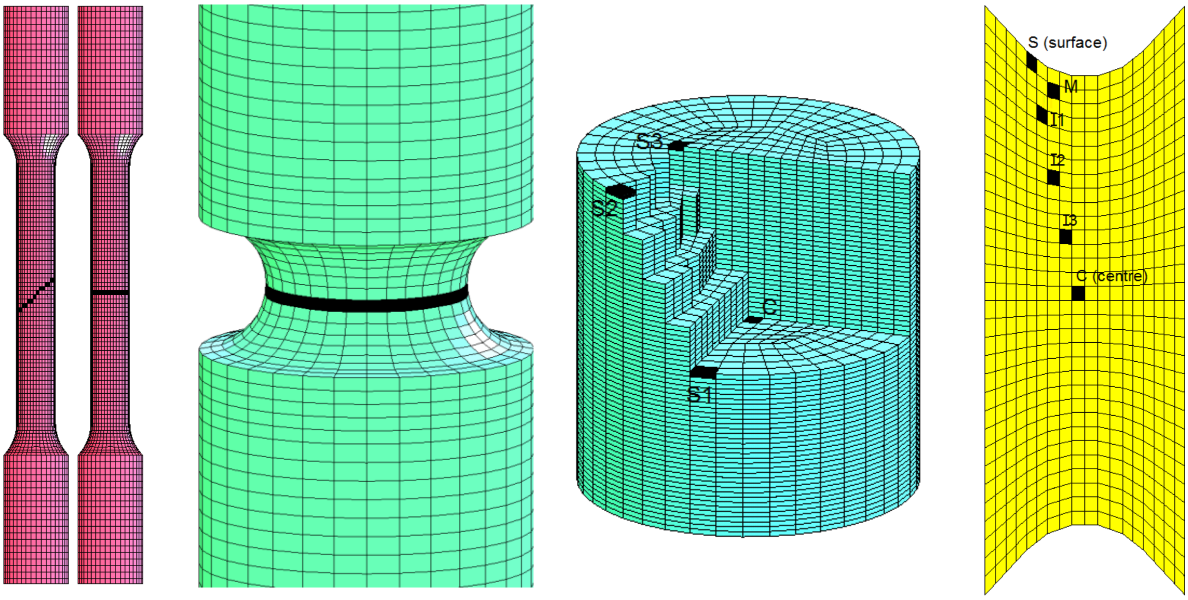

(a1) (a2) (b) (c) (d)

Figure 14

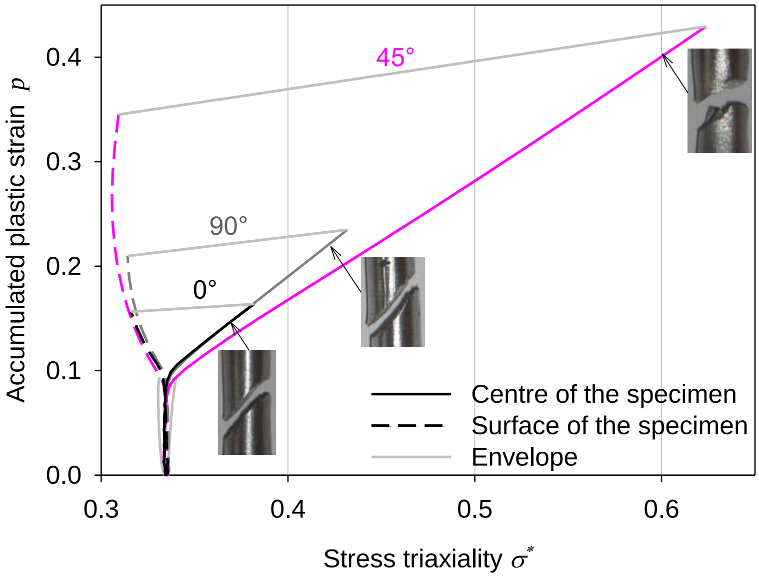

45°
90°
0°
Accumulated plastic strain p
0.0
0.1
0.2
0.3
0.4
0.3
0.4
0.5
0.6
Stress triaxiality σ^*
Centre of the specimen
Surface of the specimen
Envelope

Figure 15

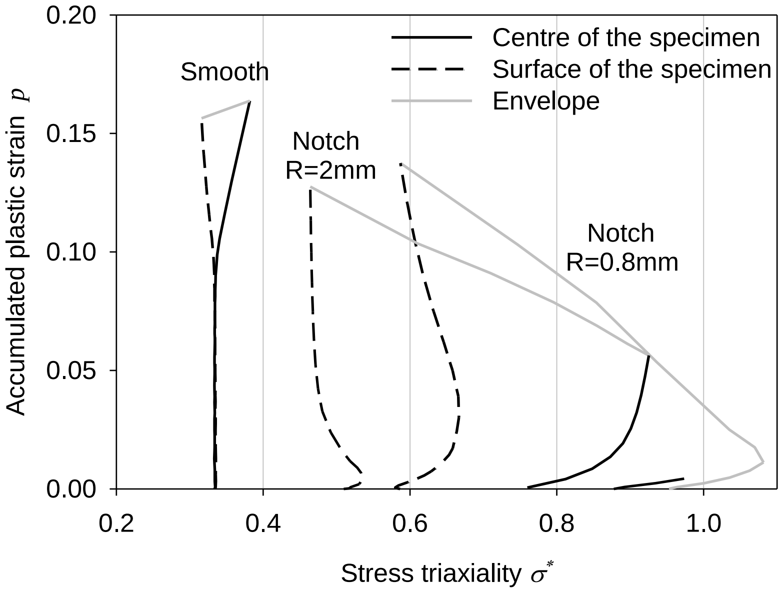
0.20
0.15
0.10
0.05
0.00
0.2
0.4
0.6
0.8
1.0
Accumulated plastic strain p
Stress triaxiality σ^*
Centre of the specimen
Surface of the specimen
Envelope
Smooth
Notch
R=2mm
Notch
R=0.8mm

Figure 16

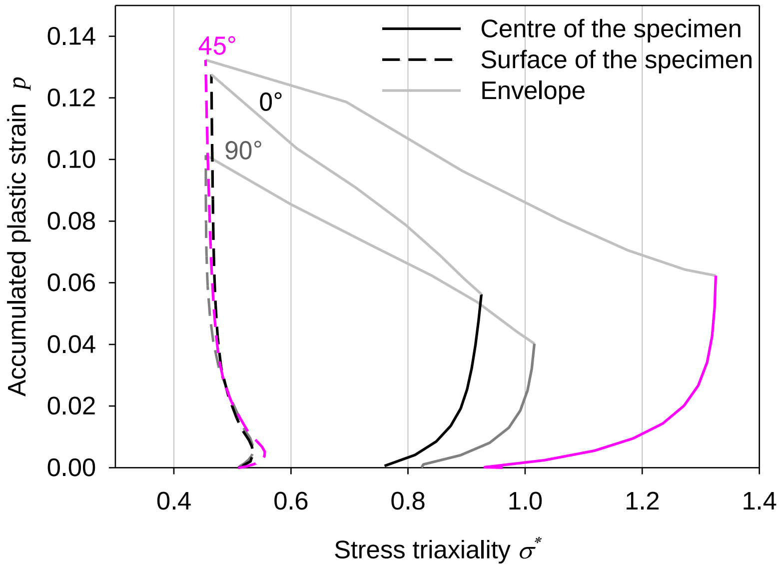
45°
0°
90°
Centre of the specimen
Surface of the specimen
Envelope
Accumulated plastic strain p
0.14
0.12
0.10
0.08
0.06
0.04
0.02
0.00
0.4
0.6
0.8
1.0
1.2
1.4
Stress triaxiality σ^*

Figure 17

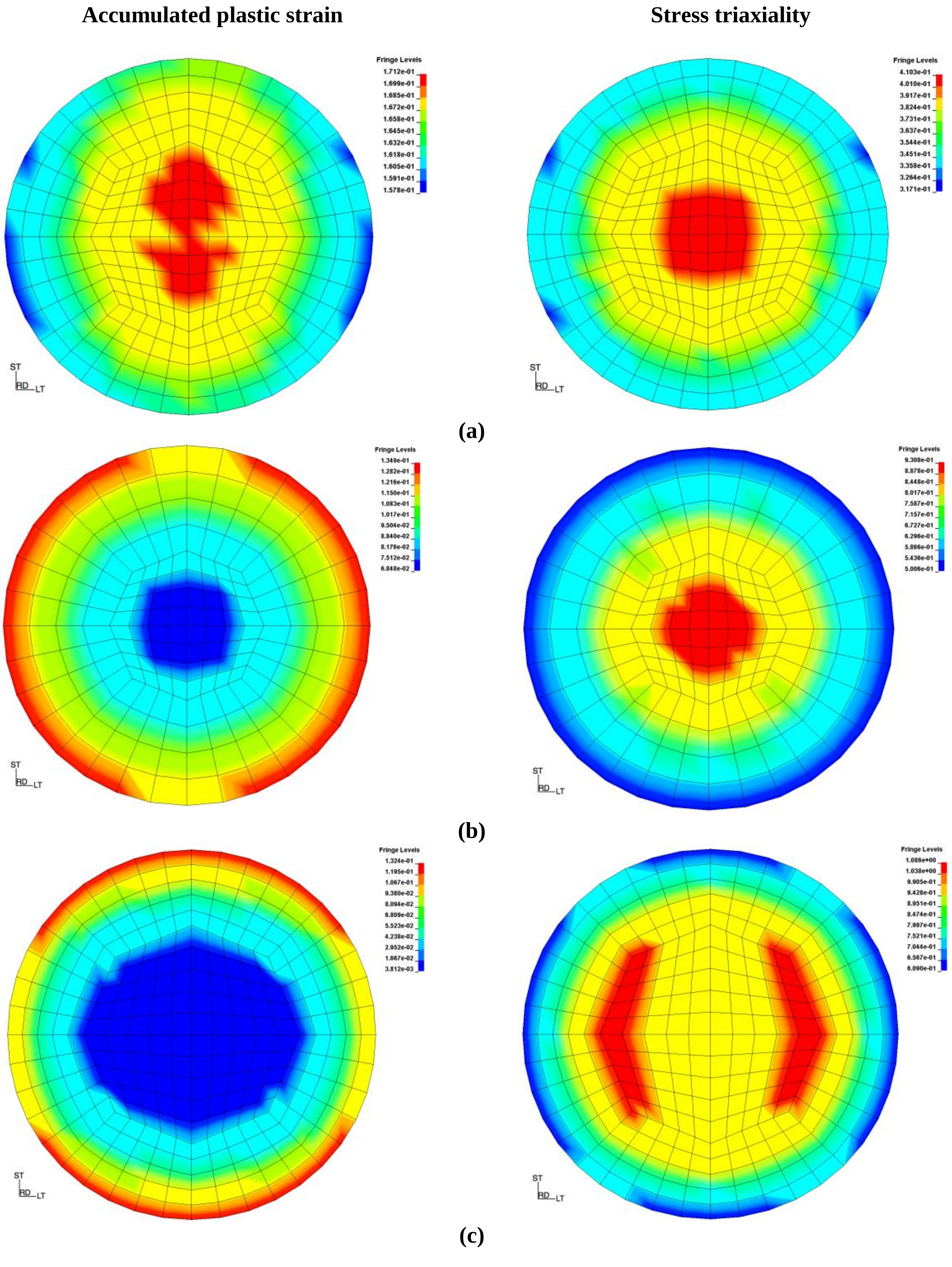

(a)

(b)

(c)

Figure 18

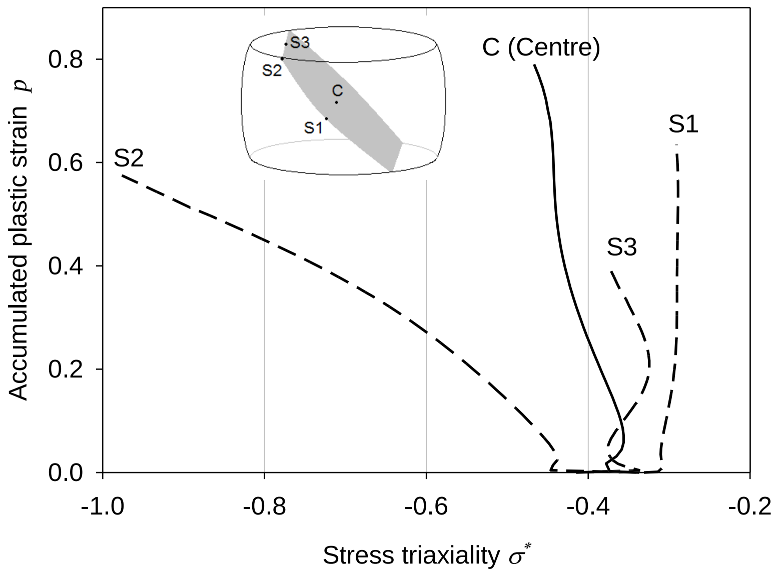

S3
S2
C
S1
C (Centre)
S1
S2
S3
0.8
0.6
0.4
0.2
0.0
Accumulated plastic strain p
-1.0
-0.8
-0.6
-0.4
-0.2
Stress triaxiality σ^*

Figure 19

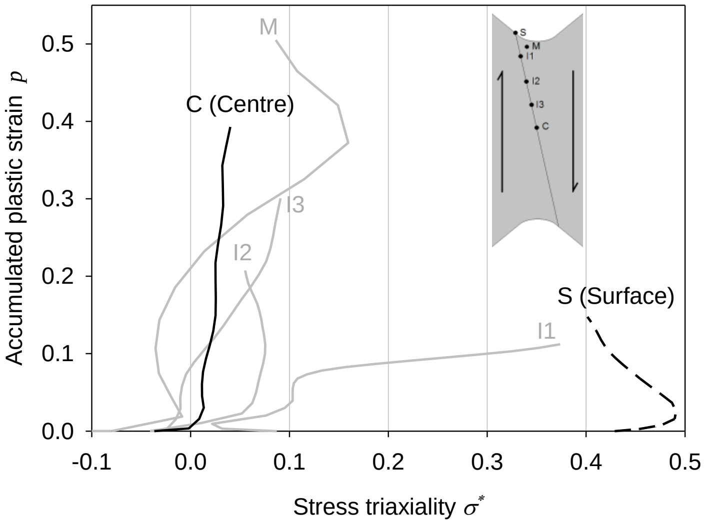
M
C (Centre)
I3
I2
S (Surface)
I1
S
M
I1
I2
I3
C
Accumulated plastic strain p
0.5
0.4
0.3
0.2
0.1
0.0
-0.1
0.0
0.1
0.2
0.3
0.4
0.5
Stress triaxiality σ^*

Figure 20

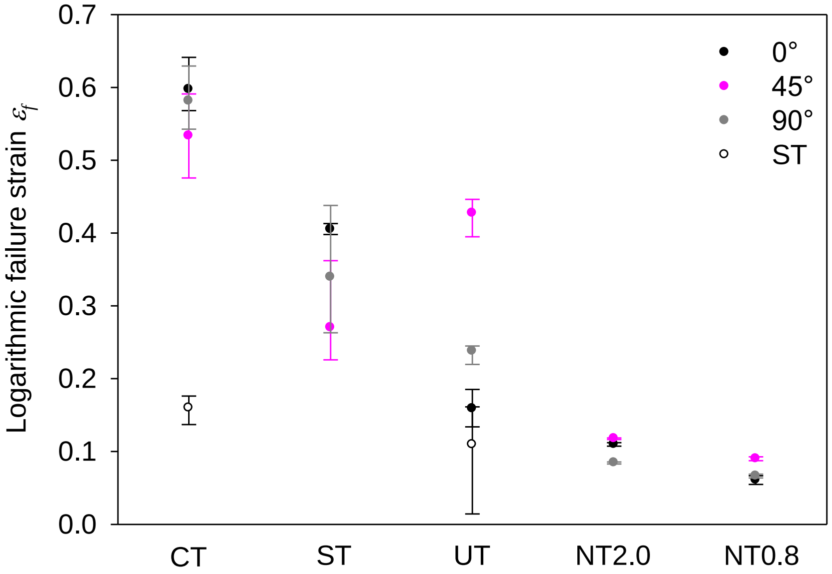
0.7
0.6
0.5
0.4
0.3
0.2
0.1
0.0
Logarithmic failure strain ε_f
CT
ST
UT
NT2.0
NT0.8
0°
45°
90°
ST